Metastable Al-Fe intermetallic stabilised by epitaxial relationship

D. Dubaux, E. Gaudry, M.-C. de Weerd, S. Šturm, M. Podlogar, J. Ghanbaja, S. Migot, V. Fournée, Muriel Sicot, J. Ledieu

Metastable Al-Fe intermetallic stabilised by epitaxial relationship

D. Dubaux[a,c], É. Gaudry[a,c], M.-C de Weerd[a,c], S. Šturm[b,c], M. Podlogar[b,c], J. Ghanbaja[a,c], S. Migot[a,c], V. Fournée[a,c], M. Sicot[a,c], J. Ledieu[a,c,*]

[a] *Université de Lorraine, CNRS, IJL, F-54000 Nancy, France*
[b] *Jožef Stefan Institute, Department for Nanostructured Materials, Jamova Cesta 39, 1000 Ljubljana, Slovenia*
[c] *International Associated Laboratory PACS2, CNRS Université de Lorraine, Nancy, France and Jožef Stefan Institute, Ljubljana, Slovenia*

Abstract

We report the adsorption of Fe for several dosing conditions on Al(100) surface held at different temperatures. For 2 monolayer equivalent of Fe deposited on the substrate held at 593 K, we observe two rotational domains of a $(\sqrt{5}\times\sqrt{5})$R26.6° structure by low energy electron diffraction and scanning tunneling microscopy. We identify this structure as the formation of the metastable Al_9Fe_2 intermetallic phase. The segregation energy and the structural stability of this intermetallic has been analysed using density functional theory based calculations. We propose that the formation of the Al_9Fe_2(001) metastable phase at the expense of other thermodynamically stable Al-Fe compounds, relies on a specific structural similarity between pure Al (001) planes of the intermetallic and Al(100) layers. These 'common' planes lead to the epitaxial relationship $(100)_{Al}\ [001]_{Al} \parallel (001)_{Al_9Fe_2}\ [1\bar{3}0]_{Al_9Fe_2}$. The Al_9Fe_2-Al matrix interface is sharp as revealed by transmission electron microscopy measurements.

Keywords: intermetallic thin film, metastable phase, segregation energy, TEM, STM, DFT

1. Introduction

When the intrinsic surface properties of materials are not compatible with the environment of use, protective coating represents an alternative solution. There exists a wealth of deposition techniques that continue to develop continuously. The choice of the most appropriate technique and of the deposited material will depend on several factors including the cost and scale of production, the desired coating functional properties, the substrate shape and the elemental constituents of the two antagonists.

Complex metallic alloys (CMA) are among the materials that have been considered as thin films due to their unique combinatorial properties. This includes low adhesion, low thermal and electrical conductivities, enhanced oxidation resistance and their potential in heterogeneous catalysis [1]. These properties orig-

*Corresponding author
Email address: Julian.ledieu@univ-lorraine.fr (J. Ledieu)

inate from the atypical chemical and structural complexities which comes from highly symmetric clusters that decorate their large to giant unit cell. Quasicrystals represent a particular sub-class of CMA with no translational symmetry, a long-range ordered structure with generally 5-fold, 10-fold or 12-fold rotational symmetries [2, 3, 4, 5]. Their multiple possible combinations offer significant prospects for innovation compared to conventional materials and find applications in diverse industrial fields (aeronautics, health, communication ...). These features explain the continuously growing interest across disciplines in studying CMA-based coating and interfaces. This is well illustrated by recent thin film developments which have integrated Al-Fe CMA phases [6, 7, 8, 9, 10].

To protect complex shaped objects with CMA coating, chemical vapour deposition represents an ideal technique. Recent works have shown the possibility to grow the $Al_{13}Fe_4$ intermetallic phase, one of the CMA identified for its catalytic properties [11]. A cross-section analysis of the coating chemical composition reveals the presence of secondary phases. The presence of Fe-rich to Al-rich phases and porosities results in many interfaces within the film. Depending on the thermal annealing selected during the chemical process, other iron aluminides (including AlFe alloy or Al_5Fe_2 CMA compound) can become the dominant phases within the thin film [6].

Due to their bulk physical and mechanical properties, Al-Fe complex intermetallics have also been considered to improve thermal barrier coating. The sequential depositions of pure Al layers and Fe-based metallic alloy powders by cold spray technique followed by a post-annealing treatment results in the formation of a multilayer intermetallic thermal barrier coatings. The alloying of Al with the stainless steel components via solid-state diffusion leads to the formation of several iron-aluminide phases including the Al_5Fe_2 complex compound around the particle cores [7]. This multilayer intermetallic coating exhibits thermal barrier properties similar to those nowadays used in low heat injection diesel engine. Here again interface reactions are key to tailor the resulting composite coating properties.

For specific deposition processes, the formation of complex intermetallics can also occur fortuitously at the coating-substrate interface. To protect steel and cast-iron parts from oxidation and corrosion, several coating processes have been developed including physical [12, 13] and chemical vapor deposition but also pack cementation [14] and hot-dipping in pure Al or Al-alloys baths [8, 9, 10]. In the case of hot-dip aluminizing, the microstructure of the resulting coating generally consists of several layers of Al-Fe intermetallics with different interfaces which *in fine* will dictate the adhesion, the lifetime and the mechanical properties of the thin film. The intermetallic phases formed between the aluminium bath and the cast-iron along with their sequence of appearance follow the Al-Fe phase diagram, here limited to its Al-rich part [15]. Starting from Al, we can identify the formation of the $Al_{13}Fe_4$ phase (also used as reinforcement particles in Al matrix composites [16, 17]), followed by the Al_5Fe_2 phase up to the cast-iron part. Once more, it is crucial to control and characterise down to the atomic scale, the intermetallic phases and the multiple interfaces formed between the steel object and the Al outer layer to expand the coating lifespan.

All these examples demonstrate the usefulness of iron-aluminide based coating for different applications [18, 19, 20, 21]. Moreover, these elements are non-critical metals and of low cost. To gain more insights into the formation of the Al-Fe CMA phases and the associated interfaces with the surrounding

matrix, an alternative approach of synthesis and characterisation has been considered. Here, we have investigated *in situ* the adsorption of Fe adatoms on a clean Al(100) surface under ultra high vacuum conditions. Many works have been previously conducted on this subject for a variety of temperatures and coverages [22, 23, 24]. The Fe growth on Al low index surfaces has been investigated using low energy electron diffraction (LEED), X-ray photoelectron spectroscopy (XPS), high energy ion scattering (HEIS), Auger electron spectroscopy (AES). The deposition of 1 to 10 monolayer equivalent (MLE) Fe on Al(111) substrate at room temperature and at 473 K result in a disordered surface layer accompanied by a disappearance of the LEED pattern. The Fe adatoms diffuse into the substrate and form an amorphous alloy layer on the surface [22]. For higher coverages, broad and faint diffraction spots suggest the formation of poorly ordered *bcc* Fe(110) islands. Anderson and Norton found that the deposition of Fe on Al(100) at room temperature leads to a rapid loss of order for low coverages (less of 1 MLE) and to the diffusion of Fe for higher coverages[24]. During the Fe deposition from 1 to 15 MLE on Al(110) and Al(001) substrates at room temperature, Shivaparan *et al.* notice that the Fe atoms displace the Al atoms from their equilibrium positions to form a mixture of FeAl up to about 5 MLE and 9 MLE respectively without diffusion into the substrates [23].

While not observed in the previous studies, we will report the growth of an Al-rich intermetallic compound on Al(100) surface. Once this moderately complex intermetallic grown, the interface and surface structures will be determined using both experimental and theoretical methods. We will demonstrate the impact of the epitaxial relationship on the selection of the grown Al-Fe phase. After describing the experimental details in Sec. 2, the experimental results will be presented in Sec. 3.1. From *ab initio* calculations, structural relaxation and segregation energy will be computed in Sec. 3.2 for different positions of Fe atom within the Al(100) region. In Sec. 3.3, the results along with an interface model are described. Finally, the Al-Fe compound and Al(100) interface will be characterised using Transmission Electronic Microscopy (TEM) analysis in Sec. 3.4. We present the discussion and conclusions in Sec. 4.

2. Experimental and Computational details

The interfaces have been prepared and characterized in a multi-chamber setup under ultra-high vacuum (base pressure under $3{\times}10^{-11}$ mbar). It is equipped with a variable temperature scanning tunneling microscope (VT-STM) operated at room temperature, LEED and XPS techniques. The STM images have been recorded in constant current mode (I_t) with positive bias (V_t) probing unoccupied states. The XPS spectra have been measured using an hemispherical analyzer and a Mg K_α X-ray source. The Al single crystal has been grown in-house by the Czochralski technique. The Al(100) surface has been prepared by repeated cycles of Ar^+ ion sputtering (1.5 keV, 15 min) and subsequent annealing to 773 K for 15 min. Sample temperatures have been monitored using an optical pyrometer with an emissivity set to 0.1. Fe thin films have been deposited by an electron beam evaporator using a high purity rod ($99.99 + at\%$). The deposition rate has been calibrated by dosing Fe on a Ag(111) substrate and by measuring the fractional area covered by STM for successive Fe depositions. The amount of Fe deposited is given in monolayer equivalent (MLE) where 1 MLE is defined as the Fe exposure needed to obtain a full monolayer

on Ag(111) at room temperature. The deposition rate was 2.2×10^{-2} MLE.s^{-1}. For cross-sectional TEM analysis, an electron-transparent lamellae has been prepared by Focus Ion Beam - Scanning Electron Microscope (FIB-SEM). Before such preparation and exposure to air, the sample has been capped with 10 MLE of Fe deposited at 300 K. The different interface structures have been analysed by High-Resolution Transmission Electron Microscopy (HRTEM), Bright-Field Scanning Transmission Electron Microscopy (BF-STEM) images and Selected Area Electron Diffraction (SAED). A composition depth profile of the lamellae has been obtained by Energy Dispersive X-ray Spectroscopy (EDXS).

Electronic structure calculations have been performed using the plane-wave Vienna *Ab initio* Simulation Package (VASP)[25, 26, 27, 28]. We have applied the spin-polarized augmented wave method (PAW) [29, 30] within the generalized gradient approximation (GGA-PBE) [31, 32] to describe the interactions between the valence electrons and the ionic core. We have considered atomic valences to be $3s^2 3p^1$ (Al) and $4s^1 3d^7$ (Fe). Total energies have been minimized until the energies differences were less than 10^{-6} eV between two electronic cycles during the structural optimizations. Atomic structures have been relaxed using conjugate gradient algorithm until the Hellmann-Feynman forces were as low as 0.03 eV/Å. Structures have been plotted using the VESTA software [33].

Slabs have been built starting from the relaxed bulk structure of *fcc* Al. The calculated Al bulk parameter (4.04 Å) was found in excellent agreement with the reported experimental data (4.05 Å) [34]. Slab calculations have been performed using a 450 eV cut-off energy (E_{cut}) and a Γ-centered $15\times15\times1$ k-grid generated according to the Monkhorst-Pack scheme [35].

To complete the XPS measurements, the core level binding energies have been investigated by DFT. The binding energy of core electrons (ECL) is calculated as the energy difference between two separate calculations in DFT [36]. The first calculation is a standard density functional calculation in which the number of core electrons corresponds to the unexcited ground state [E(n_c)]. In the second calculation one electron is removed from the core of one particular atom and added to the valence or conduction band [E(n_{c-1})]. The energy difference is a measure for the experimentally determined core-level binding energy ECL = E(n_{c-1}) - E(n_c).

3. Results

3.1. Fe adsorption on Al(100)

The STM images and LEED patterns have been recorded as a function of the substrate temperature T_{sub} and Fe coverages. Prior to Fe adsorption, a sharp (1×1) LEED pattern of the clean Al(100) surface was obtained (not shown here) corresponding in real space to a square surface unit cell with a unit mesh dimension equal to $a = 2.86$ Å ($\sqrt{2}$ times smaller than the known lattice parameter of the *fcc* crystalline structure of elemental aluminium). Upon successive dosing at $T_{sub} \geq 300$ K, the LEED pattern gradually vanishes. After 2 MLE Fe deposition at $T_{sub} \geq 593$ K, additional diffraction spots are observed as displayed in Fig.1.

Note that a similar pattern is obtained when Fe is deposited at $T_{sub} = 300$ K followed by subsequent annealing between 593 K and 793 K. Thus, the formation of the new phase is a thermally activated process and is stable up to 793 K, which is the highest annealing temperature to prepare the Al(100) substrate.

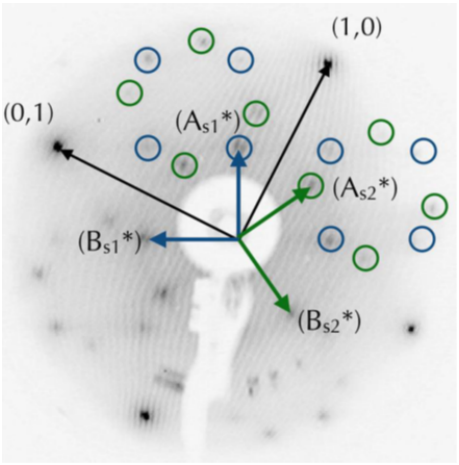

Figure 1: LEED pattern at 50 eV (in inverted colors for clarity) obtained after dosing 2 MLE Fe on the Al(100) held at 593 K. The black arrows indicate the Al(100) reciprocal lattice. The green/blue circles outline the two rotational domains of the $(\sqrt{5} \times \sqrt{5})$R26.6° phase.

The LEED pattern can be interpreted as two rotational domains of a $(\sqrt{5} \times \sqrt{5})$R26.6° phase leading to the sharp spots circled in blue and green in Fig.1. Both domains are mirror symmetric with respect to the [011] substrate direction. Each domain should be equally present at the surface as their respective spot intensities are qualitatively comparable.

Figure 2(A) displays the corresponding large scale STM image. The surface exhibits a step and terrace morphology. From this high resolution STM image and the calculated Fast Fourier Transform (see inset in Fig.2(A)), the terraces appear atomically flat and well-ordered. Contrary, the step edges are decorated by atomic clusters of various sizes and heights which lead to a relatively high degree of disorder. From the XPS measurements, these clusters cannot be associated with extrinsic impurities as only Al and Fe could be detected. Instead, they probably originate from an incomplete ordering also manifested in the low intensity of the $(\sqrt{5} \times \sqrt{5})$R26.6° LEED pattern. These STM observations (absence of dispersed nano-islands, terrace width ...) suggest the growth of a Al-Fe surface alloy as opposed to a thin Fe overlayer. This will be further confirmed by the following XPS measurements and *ab initio* calculations. As shown in Fig.2(B-C), a careful examination of the surface confirms the presence of two domains rotated by ±26.6° with respect to the substrate [011] direction. Each domain exhibits a square surface unit mesh (see white squares in Fig.2(B-C)) characterized by a lattice parameter equal to 6.3 ±0.3 Å, *i.e.* $\sqrt{5}$ times the Al(100) surface lattice parameter (a = 2.86 Å).

Following the surface structural characterisation of the thin film, the surface chemical composition has been investigated using XPS as a function of Fe coverage up to 12 MLE for T_{sub} = 593 K. Figure 3 displays the atomic percentage of Al as a function of Fe coverage, as deduced from the area of the Al $2p$ and Fe $3p$ core level spectra. From sub-monolayer equivalent coverage up to 2 MLE, the amount of Al decreases with increasing Fe exposure. For 2 MLE and above, the Al atomic concentration remains constant at 80% at.

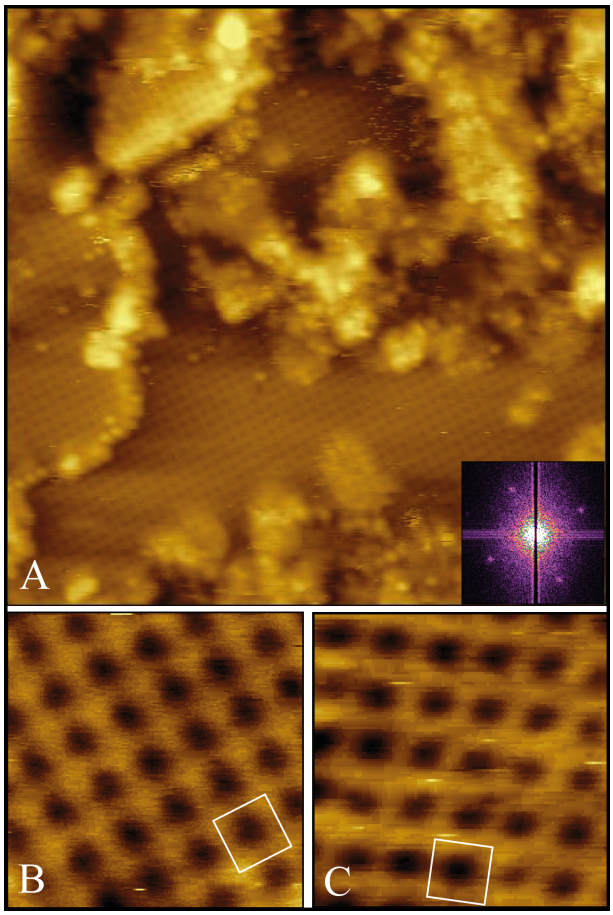

Figure 2: (A) 30 nm×30 nm high resolution STM image (V_t=-2V; I_t=0.1nA) obtained after dosing 2 MLE Fe on the Al(100) held to 593 K. Within the terraces, there is a high degree of order leading to the well defined 2D Fast Fourier Transform of the image shown in the inset. (B-C) The STM images (3.4 nm×3.4 nm) exhibit the two rotational domains of the $(\sqrt{5} \times \sqrt{5})$R26.6° phase under the same dosing conditions (V_t=2V; I_t=0.1nA). The white squares highlight the new phase unit cell.

(20% at. Fe). This implies the formation of a binary Al-Fe film which has a thickness greater than the XPS probing depth. According to Simensen *et al.* [37], this stoichiometry corresponds to the intermetallic Al_9Fe_2 phase, one of the most Al-rich metastable compounds of known Al-Fe binaries. From the uncertainty associated with XPS (±5% at.%), the $Al_{13}Fe_4$ (76% at.Al) or Al_6Fe (85% at.Al) compounds have been considered. However, the Al_9Fe_2 is the only Al-Fe intermetallic with lattice parameters matching those of the $(\sqrt{5} \times \sqrt{5})$R26.6° phase. Indeed, the monoclinic Al_9Fe_2 compound is thought to crystallise in the $P2_1/a$, P2/a or P1a space group with the following parameters: $a_{Al_9Fe_2} = 8.69$ Å, $b_{Al_9Fe_2} = 6.35$ Å, $c_{Al_9Fe_2} = 6.32$ Å and $\beta_{Al_9Fe_2} = 93.4°$ [37].

In Ref.[37], a quantitative analysis of the diffraction patterns combined with the compound stoichiometry led to the conclusion that the Al_9Fe_2 phase is isomorphous to the Al_9Co_2 compound ($P2_1/c$ space group) which is considered

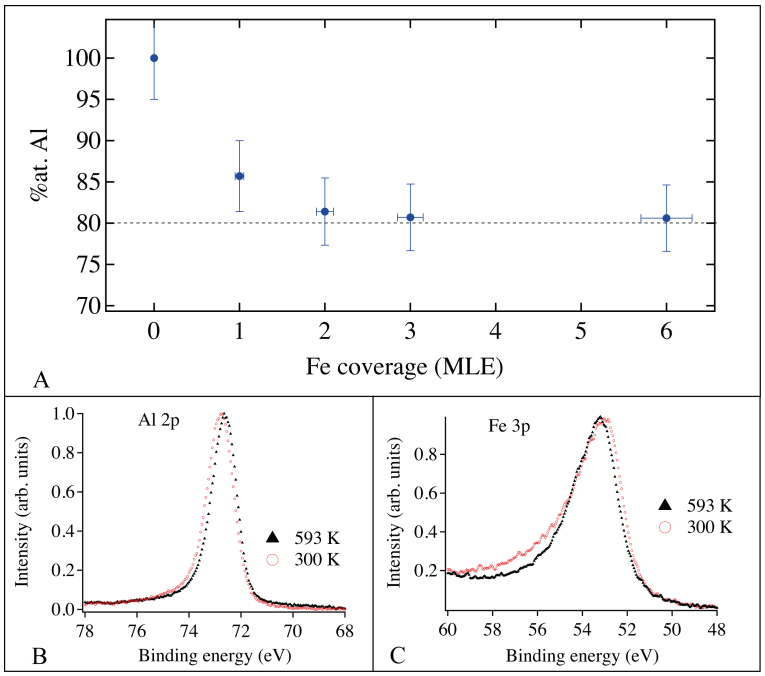

Figure 3: (A) Evolution of the Al atomic concentration measured by XPS as a function of Fe deposition with T_{sub} = 593 K. (B-C) Al 2p and Fe 3p core level spectra obtained after deposition of 2 MLE Fe at 300 K and 593 K.

as a CMA of low complexity [38]. A similar relationship is found between $Al_{13}Fe_4$ and $Al_{13}Co_4$ monoclinic structures. For the sake of comparison with previous related works on Al_9TM_2 (TM= Ir, Co) [39, 40], we have reconsidered the structure as follows: $a_{Al_9Fe_2}$ = 6.32 Å, $b_{Al_9Fe_2}$ = 6.35 Å, $c_{Al_9Fe_2}$ = 8.69 Å and $\beta_{Al_9Fe_2}$ = 93.4°. As a structural refinement is still lacking for this Al_9Fe_2 phase, this assumption allows us to describe the Al_9Fe_2 intermetallic compound in the $P2_1/c$ space group. As shown in Fig.4(left), the atomic structure can be viewed as a stacking of two atomic layers alternating along the c-axis: an almost flat (F-type) layer containing 5 Al atoms per unit cell and a more puckered layer (P-type) containing 4 Al and 2 Fe atoms per unit cell.

The Al atoms on each F and F' planes form slightly distorted square arrangements. These layers are structurally similar to Al(100) plane, although with some rumpling (see Fig.4(right)). For a given flat plane, all squares are aligned in the same direction and rotated by +/- 26.6±0.5° from the Al_9Fe_2 [100] unit cell direction. These two specific orientations of the square motifs originate from symmetry operations (a 2_1 screw axis along b or a glide operation along the c axis) that relate F and F'.

In addition to the chemical composition, XPS analysis of elemental core level spectra can provide information about the local bonding environment of the elements. The Al 2p core level energy is measured at 72.70 ±0.05 eV after 2 MLE Fe dosing at room temperature, i.e. lower in binding energy compared to the metallic state (72.85 eV) reported on clean Al(100) [41]. Upon forming the Al_9Fe_2 intermetallic, the binding energy decreases further to 72.60 eV (see

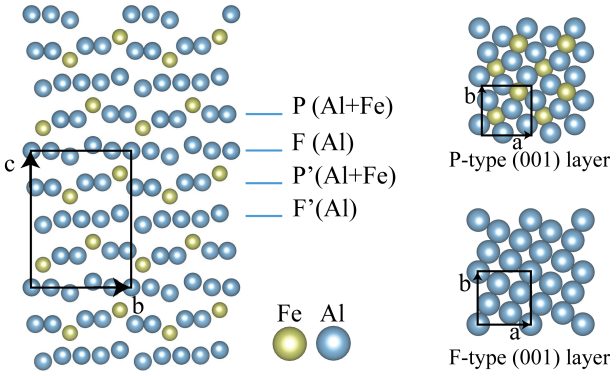

Figure 4: (Left) Representation of the Al_9Fe_2 crystal structure as a sequence of Al flat (F, F') and Al+Fe puckered (P, P') layers along the c axis. The angle between c and a axes is 93.4°. (Right) The P and F-type (001) layers are perpendicular to the [001] direction.

Fig.3B). Regarding the Fe $3p$ core level, a binding energy shift of 0.20 eV is measured between 2 MLE Fe deposited at 300 K (53.05 eV) and after annealing to 593 K (53.25 eV) (see Fig.3C). For room temperature deposition, the small Al $2p$ core level shift indicates an Al environment different to that of clean Al(100). This is supported by the absence of LEED pattern which suggests a disordered surface. Under these dosing conditions, the Fe concentration in the near-surface region would be greater than after annealing to 593 K and the system resembles to a Fe-rich disordered thin film. The binding energy is then comparable to those reported for Fe metallic state [42, 43].

Upon dosing with T_{sub} at 593 K, the increased diffusion of Fe adatoms within the substrate results in a more diluted Fe concentration in the near-surface region, hence departing from the picture of an Fe-rich thin film. From previous works on Al-TM intermetallics [39, 44], charge transfers and covalent-like interactions between Al and Fe atoms are expected for complex metallic alloys and would explain the associated higher binding energy of the Fe $3p$ core level. In addition, the core level binding energy calculated for bulk Al_9Fe_2 is also shifted to higher binding energies compared to *bcc* Fe with an energy difference of 0.42 eV. Contrary to the calculations, the structure of the Fe deposited at 300 K is not strictly speaking a *bcc* Fe and this could explain the greater shift observed between the calculated and measured core level shifts. An interesting feature lies in the core level line shapes which is more asymmetric towards the higher binding energies at 300 K than at 593 K. This asymmetry arises from electron-hole excitation across the Fermi edge upon core hole formation, the probability of the process decaying with the electron-hole pair energy [45]. Hence, the reduced asymmetry for the Fe $3p$ core level spectra of the Al_9Fe_2 intermetallic reflects a reduction of the electronic density of states (DOS) often observed in CMA [46, 47] and present in Al_9Co_2 [39]. This reduction of the DOS is confirmed by *ab initio* calculations which also highlight the presence of a pseudogap above the Fermi level (see Fig.S1).

3.2. Ab initio calculations

Following these experimental observations, the structural stability, the segregation energy and the possible Al-Fe/Al interfacial model have been investigated using *ab initio* calculations. To this end, the first step consists in determining the structural relaxation and the segregation energy for different depth of an Fe atom (in substitution of an Al atom) in Al(100). Thus, a slab of 19 layers has been built where 7 layers are fixed at the bottom and 12 layers are allowed to relax (note that the supercell parameters of the slab are fixed and only atomic relaxation occurs). This slab has been used to model the intermetallic-Al matrix interface which is the second objective here. A (001) puckered plane of Al_9Fe_2 has been positioned atop Al(100) and buried in the subsubsurface region to evaluate the plane structural stability upon relaxation and to obtain the associated segregation energy. Due to commensurability between the two antagonists, a $(\sqrt{5} \times \sqrt{5})$R26.6° surface unit cell has been considered for *fcc* Al ($\sqrt{5} \times a/\sqrt{2} =$ 6.38 Å), i.e. a square surface unit cell with a lattice mismatch smaller than 1%.

Structural relaxations have been computed for the Al slab containing one Fe atom in substitution of an Al atom into a layer labelled S-i. S ($i = 0$) stands for the surface Al(100) plane whereas S-i corresponds to the i-th layer below the surface layer S. The results reported in Fig.5(A, top) display the difference between the vertical z coordinate of the Fe atom, z_{Fe} and that of the Al plane, $z_{\mathrm{Al_{plane}}}$ in which the substitution occurs, as a function of the position (S-i) of the Fe atom in the Al slab. When located at S, Fe atom relaxes inward with a shift of 1.16 Å below the surface plane. The calculations clearly demonstrate an almost vanishing z displacement when Fe atom occupies S-i with $i \geq 2$ layers. This indicates that Fe atom remains at the same height as the neighbouring Al atoms, i.e. within the bulk plane. In this latter case, the Al-Fe atomic distance displayed in Fig.5(A, bottom) is equal to 2.73 Å corresponding to the sum of the atomic radii of the two elements ($r_{Al} = 143$ pm and $r_{Fe} = 130$ pm).

These results can be understood in the light of the segregation energy reported in Fig.5(B) which has been calculated for several S-i configurations taking the energy of the slab containing a surface Fe atom as a reference. The graph reveals an energy difference of 0.49 eV if the Fe atom is at the surface or embedded at S-2. This difference is even more pronounced (almost doubled) if the system is not relaxed with a value of 0.98 eV. The same trend is observed as the Fe atom is buried deeper into the Al slab. These results indicate that Fe atoms are unlikely to be found within the Al(100) topmost surface layer. From energetics consideration, we can consider that Fe atoms will diffuse in the sub-surface region after deposition at 300 K.

3.3. Interfacial model

To model the intermetallic and Al(100) substrate interface, we have considered two positions of a P layer of the Al_9Fe_2 compound within the Al slab, at the surface and buried as a S-2 layer (see Fig.6). The segregation energy difference between the two configurations is equal to 1.41 eV (1.98 eV) in relaxed (non-relaxed) mode. The value obtained for non-relaxed mode is well reproduced by doubling the segregation energy obtained for one Fe atom (see Fig.5(B)). This is expected as each P layer contains 2 Fe atoms per unit cell. However, this agreement is not reproduced for the relaxed mode (2×0.49 eV $<$ 1.41eV) which demonstrate the impact of the atomic relaxation and of the intermetallic structural ordering on the segregation energy. A solid-solution would have

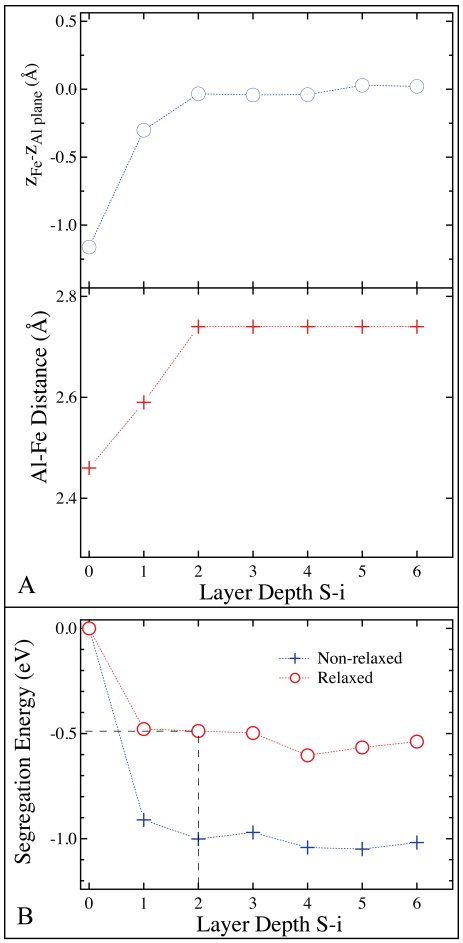

Figure 5: Structural relaxations calculated as a function of the Fe atomic position in Al(100) oriented crystal. (A, top) The quantity ($z_{\mathrm{Fe}} - z_{\mathrm{Al_{plane}}}$) and (A, bottom) the Al to Fe distance are given in Å. (B) Segregation energy (eV) evaluated for relaxed and non-relaxed slabs. The energy of the slab containing a surface Fe atom is taken as the reference energy. The Fe position in the slab is denoted by x-coordinate with 0 for surface layer (S), 1 for subsurface layer (S-1), etc.

probably resulted in a value close to 0.98 eV in relaxed mode. Finally, these calculations confirmed once more that Fe-containing layers are not favored as outermost surface planes. Moreover, Fig.6(right) reveals the large influence of an embedded P layer (S-2) on adjacent Al layers. The latter presents a large buckling then resembling a F-type plane (pure Al) of the Al_9Fe_2 compound.

3.4. Al_9Fe_2/Al(100) interface characterisation by TEM

As presented in the previous paragraphs, the adsorption of Fe on Al(100) leads to the formation of Al_9Fe_2(001) as revealed by surface techniques and DFT calculations. The Al_9Fe_2 stoichiometry is maintained for a thickness equal to at least the XPS probing depth which is estimated here around 4 nm ($3\times\lambda_{Al}$, the

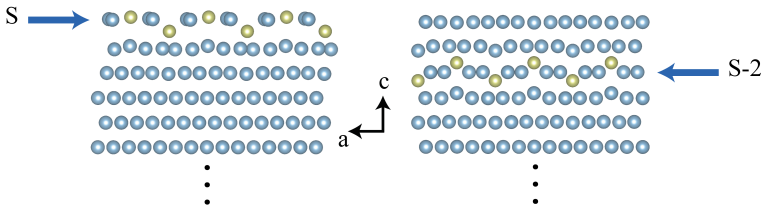

Figure 6: Side view of the Al slab with a $Al_9Fe_2(001)$ puckered plane located (left) at the surface (S) and (right) buried in the subsubsurface layer (S-2).

inelastic mean free path of the photoelectrons). However, the XPS measurements are not sufficient to assert the formation of an homogeneous intermetallic phase beneath the surface. To this end, SAED pattern analysis, atomic-resolution BF-STEM imaging combined with EDXS measurements have been carried out on a lamellae to determine the intermetallic composition and thickness after 7 MLE Fe deposition at 593 K along with the $Al_9Fe_2(001)/Al(100)$ interface structure.

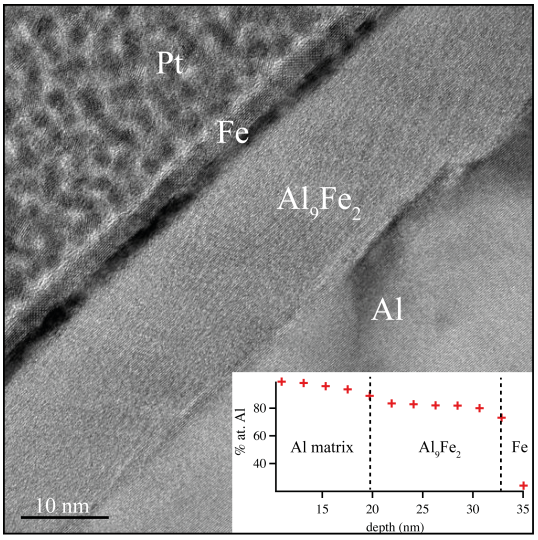

Figure 7: HRTEM image exhibiting the Fe/Al_9Fe_2 structure grown on Al(100). Inset: Al concentration profile recorded across the $Fe/Al_9Fe_2/Al$ matrix interfaces on a different part of the lamella. The composition determined by EDXS is in agreement with the formation of a 14 nm thick Al_9Fe_2 layer. Away from the interfaces which impact the measurements, an almost constant $Al_{82}Fe_{18}$ stoichiometry has been determined.

In Fig.7, cross-sectional HRTEM measurements of the lamella reveal an approximately 14 nm thick Al_9Fe_2 film on the Al(100). During the growth of the intermetallic, there is a clear Fe diffusion beneath the Al_9Fe_2/Al interface over 5 nm. The EDXS measurements confirm also that capping the $Al_9Fe_2(001)/Al(100)$ sample by 10 MLE Fe before its removal from UHV has limited oxygen diffusion into the thin film. However, the intermetallic-Fe interface is not sharp (see Fig.7) due to Fe and $Al_9Fe_2(001)$ interdiffusion. This region

of about 2 nm in thickness appears with a darker contrast between Fe and Al_9Fe_2 matrices. The maximum Al_9Fe_2 thickness was expected around 15 nm prior to Fe capping which is consistent with these observations. Regarding the SAED measurements (Fig.8), the patterns have been acquired in the $[001]_{Al}$ zone-axis. The region probed includes the Al matrix and the Al_9Fe_2/Al interface region which explains the superposition of the Al substrate and Al_9Fe_2 film zone-axis in the diffraction pattern. The analysis confirms that the $(100)_{Al}$ lattice planes are parallel to $(001)_{Al_9Fe_2}$ layers. The orientation relationship deduced from the SAED measurements is $(100)_{Al}$ $[001]_{Al}$ $\parallel$ $(001)_{Al_9Fe_2}$ $[1\bar{3}0]_{Al_9Fe_2}$. Considering the lattice parameters proposed by Simensen *et al.* [37], the theoretical lattice mismatch between $(\bar{3}\bar{1}0)_{Al_9Fe_2}$ and $(020)_{Al}$ is 0.8%.

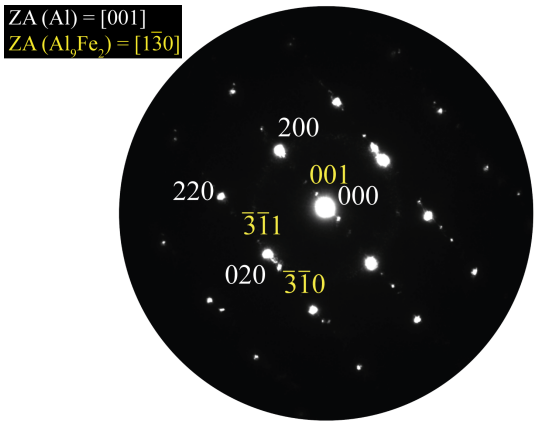

Figure 8: SAED pattern acquired over an area including the Al matrix and the intermetallic. The latter are viewed in the $[001]_{Al}$ and $[1\bar{3}0]_{Al_9Fe_2}$ zone axis respectively.

Figure 9 presents atomic-resolution BF-STEM filtered image of the Al_9Fe_2/Al interface viewed along the $[001]_{Al}$ and $[1\bar{3}0]_{Al_9Fe_2}$ zone axis, respectively. To confirm that the image processing did not introduce any additional artefact, the original BF-STEM image is shown in a rectangle in the right hand side image section. The atomically flat interfacial region is marked by a dashed line, which separates the Al substrate from the Al_9Fe_2 intermetallic. The corresponding superimposed atomic models are in decent agreement with the underlying atomic-resolution image. The atomic columns in Al substrate are represented in a square-like pattern of discrete dots of high contrast. As a first approximation, the intermetallic phase has been built by considering the reported lattice parameters of Al_9Fe_2 [37] and a phase isomorphic to the Al_9Co_2 compound. In the observed projection, the a and c crystallographic axis of the Al_9Fe_2 phase are orientated parallel and nearly perpendicular to the interface plane, respectively. The atomic structure when observed perpendicular to the interface is marked by alternating Al layers (F-type) and mixed puckered Al-Fe layers (P-type). The contrast variation and a stacking motif across the interface confirms that the first atomic plane of the Al_9Fe_2 intermetallic is associated with the F-type plane composed of Al atoms, which are structurally similar to the Al(100) plane in the substrate. The predicted puckered Al planes of the Al_9Fe_2 intermetallic interfacing with the Al substrate is clearly visible in the experimental image just

across the interface, the last Al columns of the intermetallic being associated to slightly elongated blurred contrasts.

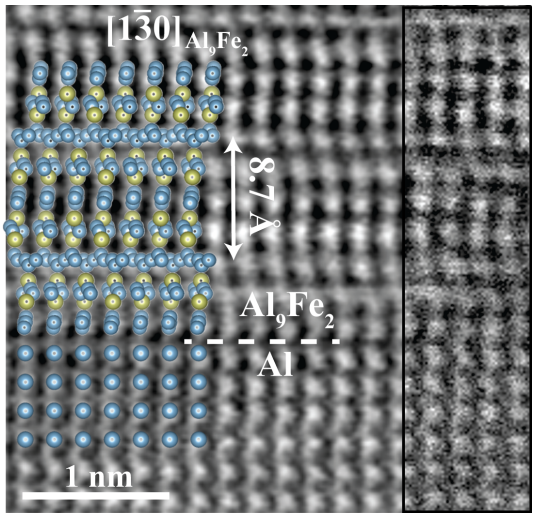

Figure 9: (Left) Atomically resolved filtered BF-STEM image of the Al_9Fe_2/Al interface region with the superimposed structural models viewed in the $[001]_{Al}$ and $[1\bar{3}0]_{Al_9Fe_2}$ zone axis respectively. (Right) Original BF-STEM image.

4. Discussion and Conclusion

Following the work of Buchanan *et al.* [48], an important intermixing length is expected when adsorbing Fe adatoms on an Al substrate at 300 K. The intermixing length is in fact greater than for the reverse configuration, i.e. Al deposited on a Fe substrate. From the elemental surface energies of both Al (1.3 J.m^{-2}) and Fe (2.2 J.m^{-2}) [49], one would expect Fe adatom diffusion in the Al(100) sub-surface region, most likely via a place-exchange mechanism. This Fe adatom diffusion into the Al matrix is further supported by *ab initio* calculations which demonstrates that Fe adatoms are energetically unfavorable at Al(100) surface. As observed experimentally and in agreement with these results, a disordered surface structure is obtained when adsorption of Fe occurs on Al(100) at room temperature.

When adsorbing at least 2 MLE Fe on Al(100) held at or slightly above 593 K, the successful growth of a Al_9Fe_2 thin film has been achieved. The measured surface lattice parameters and composition are in agreement with those reported previously [37]. The (001) oriented Al_9Fe_2 surface is bulk-terminated at pure Al planes as supported by *ab initio* calculations. Both surface and interface analysis reveal a coherent growth of the Al_9Fe_2 compound on the Al(100) crystal with a relatively sharp interface. Although metastable, the Al_9Fe_2 compound is the only phase formed up to 20 MLE Fe between 593 K and 773 K, i.e. stable up to the annealing temperature of the Al(100) clean surface. Interestingly, the metastable Al_9Fe_2 phase has been reported only when studying the microstructure of strip cast material of Al-0.5 Wt.% Fe-0.2 Wt.% Si alloy,

i.e. for a rapidly solidified material [37]. For Al-Fe hypoeutectic alloys, it is proposed that the formation of other phases will prevail at lower cooling rates [50]. It is then highly surprising to grow under the present conditions the Al_9Fe_2 phase at the Al(100) surface. Indeed, the formation of the $Al_{13}Fe_4$ and Al_6Fe compounds could have been expected being respectively the Al-richest stable and metastable phases in the Al-Fe binary system.

When adsorbing Ir atoms on Al(100) under similar conditions, recent works [40] have highlighted the growth of an (001) oriented Al_9Ir_2 thin film. Like the Al_9Fe_2, this intermetallic is isostructural to the Al_9Co_2 compound. More importantly, it is a stable phase which corresponds to the Al-richest phase in the Al-Ir binary system. Regardless of the thermodynamic stability of the phase, the growth of stable or metastable Al_9TM_2 phases is achieved on Al(100). As a small amount of TM is adsorbed on a large amount of Al, could it simply rely on growing first the Al-richest phases in their respective binary system? While verified for the Al-Ir system, the formation of the metastable orthorhombic Al_6Fe phase [51, 52] should have occurred. In addition, if the growth of Al_9TM_2 phases on Al(100) relies simply on reaching the right stoichiometry, it should be possible to grow similar intermetallic compounds on other Al low index surfaces. This has not been achieved yet. Under comparable preparation and dosing conditions (2 MLE), we have investigated Fe adsorption on Al(111) from room temperature up to 600 K. Like others [22] in the low dosing regime, no ordering could be detected except for a fainting three-fold LEED pattern.

Consequently, additional factors to the film chemistry must influence the growth of the Al_9TM_2 compound. We now recall the bulk structure of the Al_9Fe_2 compound (see Fig.4). Along the c-axis, half of the Al_9Fe_2 bulk planes (the F-type in Fig.10) can be regarded as rumpled "Al(100)" layers. During the growth of the Al_9Fe_2 phase, a minimal restructuring of the (100) Al planes would be required to form F and F' layers. In comparison, a substantial reordering will occur to form P-type layers which are composed of 4 Al and 2 Fe atoms per unit cell. Nevertheless, this moderate atomic rearrangement could translate into a lower energetic cost associated with the formation of Al_9Fe_2 phase on Al(100) compared to the $Al_{13}Fe_4$ compound, the latter structure consisting of columns of 23-atom pentagonal pyramid clusters propagating along the [010] direction [53].

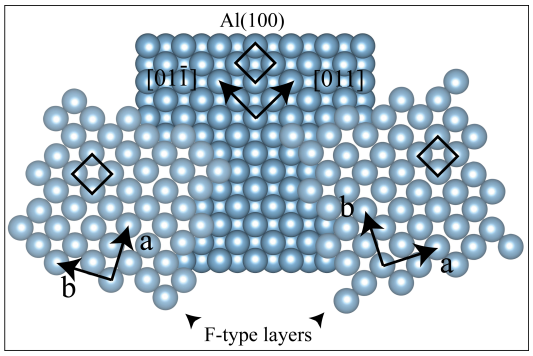

Figure 10: Visualisation of the interface alignement between F-type layers with the Al(100) surface. This configuration will generate the LEED pattern described as $(\sqrt{5} \times \sqrt{5})$R26.6°.

At the Al-intermetallic interface, the two antagonists will be the (100) Al and (001) F-type planes. As depicted in Fig.10, the alignment of the Al square motifs present in F-type layers with those of the Al(100) surface imposes a rotation of the intermetallic unit cell of $\pm 26.6°$ with respect to the substrate. The two orientations originate from the symmetry operation that relates F/F' layers within the unit cell and will generate mirror symmetric domains with respect to the substrate [011] direction, indistinguishable in the LEED pattern due to a coincidence of the diffraction spots.

To conclude, we propose that the epitaxial relationship generated by these 'common' Al layers is a necessary condition for the growth of the Al_9Fe_2 compound. It is also this particular structural resemblance between (100) and F-type planes that dictates the growth direction of the intermetallic, here an (001) oriented intermetallic. With no such relationship between Al(111) and Al_9Fe_2 planes, the growth of the intermetallic has not been reached. From the Al-Fe phase diagram, it is foreseen that a higher annealing temperature would lead to the growth of the $Al_{13}Fe_4$ compound, possibility limited here by the substrate melting temperature.

Finally, the growth of the Al_9Fe_2 compound as thin film offers an opportunity to explore its associated physical and chemical surface properties and its potential use as protective or functional coating. Moreover, this work offers a new approach to the synthesis of metastable and stable intermetallics as surface alloy, based on the structural coincidence between substrate and intermetallic bulk layers. This concept should now be applied first, to other Al-rich intermetallic compounds and for other Al surface orientations and second, to different binary systems.

Supporting Information Available

Supporting Information: Bulk partial and total density of states of Al_9Fe_2.

Declaration of Competing Interests

The authors declare that they have no known competing financial interests or personal relationships that could have appeared to influence the work reported in this paper.

Acknowledgements

J.L. acknowledges financial support from the Conseil Régional of Région Grand-Est. This work is a result of cooperation within the European C-MAC and within the French-Slovene collaboration established under Push-Pull Alloys and Complex Compounds ($PACS_2$) Joint Open Laboratory. We thanks the CENN Nanocenter for the use of FIB-SEM. E.G acknowledges financial support through the COMETE project (COnception in silico de Matériaux pour l'EnvironnemenT et l'Energie) cofunded by the European Union under the program FEDER-FSE Lorraine et Massif des Vosges 2014-2020. High Performance Computing resources were provided by GENCI under the allocation 99642 (IDRIS, CINES and TGCC centers), and by the EXPLOR center hosted by the Université de Lorraine (allocation 2017M4XXX0108).

References

[1] J. Dubois, Properties- and applications of quasicrystals and complex metallic alloys, Chem. Soc. Rev. 41 (2012) 6760–6777.

[2] D. Shechtman, I. Blech, D. Gratias, J. Cahn, Metallic Phase with Long-Range Orientational Order and No Translational Symmetry, Phys. Rev. Lett. 53 (1984) 1951–1953.

[3] B. Dubost, J. Lang, M. Tanaka, P. Sainfort, Large AlCuLi Single Quasicrystals with Triacontahedral Solidification Morphology, Nature 324 (1986) 48–50.

[4] A. Tsai, A. Inoue, Y. Yokoyama, T. Masumoto, Stable Icosahedral Al-Pd-Mn and Al-Pd-Re Alloys, Mater. Trans., JIM 31 (1990) 98–103.

[5] S. Förster, K. Meinel, R. Hammer, M. Trautmann, W. Widdra, Quasicrystalline Structure Formation in a Classical Crystalline Thin-Film System, Nature 502 (2013) 215–218.

[6] I. Aviziotis, T. Duguet, K. Soussi, M. Heggen, M. Lafont, F. Morfin, S. Mishra, S. Daniele, A. Boudouvis, C. Vahlas, Chemical Vapor Deposition of $Al_{13}Fe_4$ Highly Selective Catalytic Films for the Semi-Hydrogenation of Acetylene, Phys. Status Solidi A 215 (2018) 1700692–(1-8).

[7] E. Leshchinsky, A. Sobiesiak, R. Maev, Intermetallic Al-, Fe-, Co-, and Ni-Based Thermal Barrier Coatings Prepared by Cold Spray for Applications on Low Heat Rejection Diesel Engines, J. Therm. Spray Technol. 27 (2018) 456–470.

[8] R. Mola, T. Bucki, K. Wcisło, Characterization of Coatings on Grey Cast Iron Fabricated by Hot-dipping in Pure Al, $AlSi_{11}$ and $AlTi_5$ Alloys, Arch. Foundry Eng. 14 (2014) 85–90.

[9] M. Abro, D. Lee, Effect of Al Hot-Dipping on High-Temperature Corrosion of Carbon Steel in N_2/0.1% H_2S Gas, Metals 6 (2016) 1–7.

[10] Z. Shamsu, N. Othman, A. Daud, M. Daud, Properties and Growth Rate of Intermetallic Al-Fe Through Hot Dipped Aluminizing, Adv. Mat. Res. 980 (2014) 3–7.

[11] M. Armbrüster, K. Kovnir, M. Friedrich, D. Teschner, G. Wowsnick, M. Hahne, P. Gille, L. Szentmiklósi, M. Feuerbacher, M. Heggen, F. Girsdies, D. Rosenthal, R. Schlögl, Yu. Grin, $Al_{13}Fe_4$ as Low-Cost Alternative for Palladium in Heterogeneous Hydrogenation, Nat. Mater. 11 (2012) 690–693.

[12] J. Qian, M. Laberge, L. Martinu, J. Klemberg-Sapieha, F. Pougoum, Z. Zhou, K. Li, S. Savoie, R. Schulz, Investigation of Fe_3Al-Based PVD/HVOF Duplex Coatings to Protect Stainless Steel from Sliding Wear against Alumina, Surf. Coat. Technol. 350 (2018) 699–711.

[13] H. Scheerer, G. Andersohn, M. Oechsner, J. Vega, H. Scheerer, G. Andersohn, M. Oechsner, Evaluation of the Open Porosity of PVD Coatings through Electrochemical Iron Detection, Surf. Coat. Technol. 350 (2018-09) 453–461.

[14] N. Krasaelom, T. Thublaor, S. Leelachao, S. Chandra-Ambhorn, High Temperature Corrosion Behaviour of Aluminised FC 25 Cast Iron using Pack Cementation, Anti-Corros. Methods Mater. 66 (2019) 236–241.

[15] X. Li, A. Scherf, M. Heilmaier, F. Stein, The Al-rich Part of the Al-Fe Phase Diagram, J. Phase Equilib. Diffus. 37 (2016) 162–173.

[16] K. Lee, W. Worrell, High-Temperature Antioxidant Multi-Layer Composite Coating on Surface of Carbon-Based Material and Preparation Method of Coating, Oxid. Met. 32 (1989) 357–369.

[17] J. Lee, S. Kang, T. Sato, H. Tezuka, A. Kamio, Fabrication of Al/Al_3Fe Composites by Plasma Synthesis Method, Mater. Sci. Eng. A 343 (2003) 199–209.

[18] P. Blau, H. Meyer, Characteristics of Wear Particles Produced during Friction Tests of Conventional and Non-Conventional Disc Brake Materials, Wear 255 (2003) 1261–1269.

[19] N. Stoloff, C.T. Liu, S.C. Deevi, Emerging Applications of Intermetallics, Intermetallics 8 (2000) 1313–1320.

[20] I. Baker, P. Munroe, Mecanical Properties of FeAl, Int. Mater. Rev. 42 (1997) 181–205.

[21] V. Sundararajan, B.R. Sahu, D.G. Kanhere, P.V. Panat, G.P. Das, Cohesive, Electronic and Magnetic Properties of the Transition Metal Aluminides FeAl, CoAl and NiAl, J. Phys.: Condens. Matter 7 (1995) 6019–6034.

[22] A. Begley, D. Tian, F. Jona, P. Marcus, Study of Ultrathin Fe Films on Pd{111}, Ag{111} and Al{111}, Surf. Sci. 280 (1993) 289–297.

[23] N. Shivaparan, V. Kraseman, V. Shutthanandan, R. Smith, Growth of Ultrathin Pd Films on Al(001) Surfaces, Surf. Sci. 365 (1996) 78–86.

[24] G.W. Anderson, P.R. Norton, The structure and magnetic properties of Fe deposited on Al(100), Surf. Sci. 336 (1995) 262–268.

[25] G. Kresse, J. Hafner, *Ab initio* molecular dynamics for liquid metals, Phys. Rev. B: Condens. Matter Mater. Phys. 47 (1993) 558–561.

[26] G. Kresse, J. Hafner, *Ab initio* Molecular-Dynamics Simulation of the Liquid-Metal-Amorphous-Semiconductor Transition in Germanium, Phys. Rev. B: Condens. Matter Mater. Phys. 49 (1994) 14251–14269.

[27] G. Kresse, J. Furthmüller, Efficient Iterative Shemes for *Ab Initio* Total-Energy Calculations using a Plane-Wave Basis Set, Phys. Rev. B: Condens. Matter Mater. Phys. 54 (1996) 11169–11186.

[28] G. Kresse, J. Furthmüller, Efficiency of *Ab Initio* Total-Energy Calculations for Metals and Semiconductors using a Plane-Wave Basis Set, Comput. Mater. Sci. 6 (1996) 15–50.

[29] P.E. Blöchl, Projector Augmented-Wave Method, Phys. Rev. B: Condens. Matter Mater. Phys. 50 (1994) 17953–17979.

[30] G. Kresse, D. Joubert, From Ultrasoft Pseudopotentials to the Projector Augmented-Wave Method, Phys. Rev. B: Condens. Matter Mater. Phys. 59 (1999) 1758–1775.

[31] J. Perdew, K. Burke, M. Ernzerhof, Generalized Gradient Approximation Made Simple, Phys. Rev. Lett. 77 (1996) 3865–3868.

[32] J. Perdew, K. Burke, M. Ernzerhof, Generalized Gradient Approximation Made Simple., Phys. Rev. Lett. 78 (1997) 1396.

[33] K. Momma, F. Izumi, Vesta 3 for Three-Dimensional Visualization of Crystal, Volumetric, a Morphology Data, J. Appl. Crystallogr. 44 (2000) 1272–1276.

[34] A. Cooper, Precise Lattice Constants of Germanium, Aluminium, Gallium Arsenide, Uranium, Sulphur, Quartz and Sapphire, Acta Crystallogr., Sect. C: Cryst. Struct. Commun. 78 (1962) 1396.

[35] H.J. Monkhorst, J.D. Pack, Special Points for Brillouin-Zone Integrations, Phys. Rev. B: Condens. Matter Mater. Phys. 78 (1976) 5188–5192.

[36] S. Lizzit, A. Baraldi, A. Groso, K. Reuter, M.V. Ganduglia-Pirovano, C. Stampfl, M. Scheffler, M. Stichler, C. Keller, W. Wurth, D. Menze, Surface Core-Level Shifts of Clean and Oxygen-Covered Ru(0001), Phys. Rev. B: Condens. Matter Mater. Phys. 63 (2001) 205419–(1-14).

[37] C.J. Simensen, R. Vellasamy, Determination of Phases Present in Cast Material of an Al-0.5 Wt.% Fe-0.2 Wt.% Si Alloy., Z. Metallkde., 68 (1977) 428–432.

[38] M. Boström, H. Rosner, Y. Prots, U. Burkhardt, Y. Grin, The Co_2Al_9 Structure Type Revisited, Z. Anorg. Allg. Chem. 631 (2005) 534–541.

[39] S. Alarcón-Villaseca, J. Ledieu, L. Serkovic-Loli, M.-C. de Weerd, P. Gille, V. Fournée, J.-M. Dubois, E. Gaudry, Structural Investigation of the (001) Surface of the Al_9Co_2 Complex Metallic Alloy, J. Phys. Chem. C 115 (2011) 14922–14932.

[40] J. Kadok, K. Pussi, S. Šturm, B. Ambrožič,E. Gaudry, M.-C. de Weerd, V. Fournée, J. Ledieu, Epitaxial Growth of Al_9Ir_2 Intermetallic Compound on Al(100): Mechanism and Interface Structure, Phys. Rev. Mater. 2 (2018) 043405–(1-9).

[41] C. Godet, V.M. Santana, D. David, Depth Distribution of Noble Gas Atoms Implanted in Al Matrix : a Photoelectron Energy Loss Spectroscopy Study, Thin solid films 659 (2018) 70–80.

[42] K. Asami, K. Hashimoto, The X-ray Photo-Electron Spectra of Several Oxides of Iron and Chromium, Corros. Sci. 17 (1977) 559–570.

[43] P. Mills, J. Sullivan, A Study of the Core-Level Electrons in Iron and its Three Oxides by Means of X-ray Photoelectron Spectroscopy, J. Phys. D: Appl. Phys. 16 (1983) 723–732.

[44] P. Scheid, C. Chatelier, J. Ledieu, V. Fournée, E. Gaudry, Bonding Network and Stability of Clusters: the Case Study of $Al_{13}TM_4$ Pseudo-Tenfold Surfaces, Acta Crystallogr., Sect. A: Found. Adv. A75 (2019) 314–324.

[45] G.D. Mahan, Excitons in Metals : Infinite Hole Mass, Phys. Rev. 163 (1967) 612–617.

[46] C. Jenks, S.-L. Chang, J. Anderegg, P. Thiel, D. Lynch, Photoelectron Spectra of an $Al_{70}Pd_{21}Mn_9$ Quasicrystal and the Cubic Alloy $Al_{60}Pd_{25}Mn_{15}$, Phys. Rev. B: Condens. Matter Mater. Phys. 54 (1996) 6301–6306.

[47] V. Fournée, J. Anderegg, A. Ross, T. Lograsso, P. Thiel, Electronic Structure of Quasicrystals Deduced from Auger and X-ray Photoelectron Spectroscopies, J. Phys.: Condens. Matter 14 (2002) 2691–2703.

[48] J. Buchanan, T. Hase, B. Tanner, P. Chen, L. Gan, C. Powell, W. Egelhoff, Anomalously Large Intermixing in Aluminium-Transition-Metal Bilayers, Phys. Rev. B: Condens. Matter Mater. Phys. 66 (2002) 104427–1 104427–5.

[49] V. Levy, P. Regnier, Mesure des Energies de Surface, Journal de Physique Colloques 31 (1970) C1-159–C1-173.

[50] R. Young, T. Clyne, An Al-Fe Intermetallic Phase Formed during Controlled Solidification, Scr. Metall. 15 (1981) 1211–1216.

[51] E. Hollingsworth, G. Frank, R. Willett, Identification of a New Al-Fe Constituent, Al_6Fe, Trans. AIME 224 (1962) 188–189.

[52] L Walford, The Structure of the Intermetallic Phase $FeAl_6$., Acta Cryst. 18 (1965) 287–291.

[53] C.L. Henley, Current Models of Decagonal Atomic Structure, J. Non-Cryst. Solids 153-154 (1993) 172–176.

Supporting Information
Metastable Al-Fe intermetallic stabilised by epitaxial relationship

D. Dubaux[a,c], É. Gaudry[a,c], M.-C de Weerd[a,c], S. Šturm[b,c], M. Podlogar[b,c], J. Ghanbaja[a,c], S. Migot[a,c], V. Fournée[a,c], M. Sicot[a,c], J. Ledieu[a,c,*]

[a] *Université de Lorraine, CNRS, IJL, F-54000 Nancy, France*
[b] *Jožef Stefan Institute, Department for Nanostructured Materials, Jamova Cesta 39, 1000 Ljubljana, Slovenia*
[c] *International Associated Laboratory PACS2, CNRS Université de Lorraine, Nancy, France and Jožef Stefan Institute, Ljubljana, Slovenia*

1. Bulk partial and total density of states of Al_9Fe_2

The partial and total electronic density of states (DOS) have been calculated for the bulk Al_9Fe_2 compound using DFT methods (see Fig.S1). The Fermi energy is taken as the origin for the binding energies. The total DOS is dominated by *sp* states below -3 eV, while the main contribution comes from Fe *d*-states between -3 eV and 0.3 eV. The presence of sharp peaks in the Al *s* and *p* states coinciding with the Fe *spd* states suggest an *sp-d* hybridization. The latter plays an important role in the pseudogap formation: the total density of states presents such minimum in the DOS lying to the right hand side of the Fermi energy.

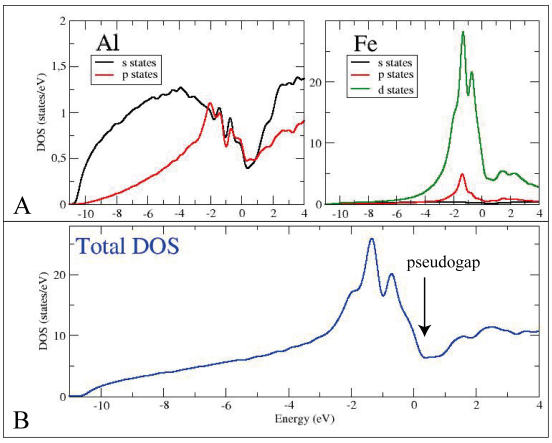

Figure S1: Calculated partial (A) and (B) total density of states (DOS) of bulk Al_9Fe_2 compound.

*Corresponding author
Email address: Julian.ledieu@univ-lorraine.fr (J. Ledieu)

The Al_9Fe_2 compound, like the Al_9Co_2 intermetallic, appears to be stabilised by a Hume-Rothery effect combined with *spd* hybridization. Using the valence reported in Ref. [1], the electron density for Al_9Fe_2 is calculated at 2.65 e/a with a unit cell volume [2] equal to 348.13 $Å^3$. Then, we deduce a diameter for the Fermi sphere equal to $2k_F = 3.41Å^{-1}$. The nearest reciprocal lattice vector of high intensity fulfilling the pseudo-Brillouin zone-Fermi - sphere surface (Hume-Rothery condition $K_{hkl}=2k_F$) contact lies at $2k_F = 3.21Å^{-1}$. It corresponds to the $(13\bar{1})$ planes.

References

[1] U. Mizutani, H. Sato, M. Inukai, Y. Nishino, E. Zijlstra, Electrons per Atom Ratio Determination and Hume-Rothery Electron Concentration Rule for P-Based Polar Compounds Studied by FLAPW - Fourier Calculations, Inorg. Chem. 54 (2015) 930-946.

[2] C.J. Simensen, R. Vellasamy, Determination of Phases Present in Cast Material of an Al-0.5 Wt.% Fe-0.2 Wt.% Si Alloy, Z. Metallkde. 68 (1977) 428–432.